

Microtechnology Department

Head: Gábor BATTISTIG Ph.D.	
Research Staff <ul style="list-style-type: none"> • István BÁRSONY, Member of HAS., • László DÓZSA, Ph.D., • Péter FÜRJES, Ph.D., • Zoltán LÁBADI, Ph.D., • György MOLNÁR, Ph.D., • Anita PONGRÁCZ, Ph.D., • Vilmos RAKOVICS, Ph.D., • Zsolt ZOLNAI, Ph.D. • Ágoston NÉMETH, Ph.D., (on leave) • Péter BASA, Ph.D., (left) • Andrea Edit PAP, Ph.D., (part time) • Antalné ÁDÁM, M.Sc., (part time) • Albert KARACS, M.Sc., (part time) • Tibor MOHÁCSY, M.Sc., (part time) • Ákos NEMCSICS, Ph.D. (part time) • Gábor PETŐ, D.Sc., Prof. Emeritus • István PINTÉR, Ph.D., (part time) • Bálint PÖDÖR, Ph.D. (part time) • Zsolt József HORVÁTH, D.Sc., (part time) • Béla SZENTPÁLI, Ph.D., (part time) • Éva VÁZSONYI, M.Sc., (part time) 	Technical Staff <ul style="list-style-type: none"> • György ALTMANN, technician • Edvard BADALJÁN, engineer • Gabriella BIRÓ, technician • Sándor CSARNAI, technician • Ábel DEBRECZENY, engineer • Magdolna ERŐS, technician • Csilla ARIAS-SOTONÉ FARAGÓ, technician • János FERENCZ, engineer • Róbert HODOVÁN, engineer • Csaba LÁZÁR, engineer • András LŐRINCZ, engineer • Ákos MAJOROS, engineer • Attila NAGY, technician • Károlyné PÁYER, technician • István RÉTI, engineer • Ádám SZENDREY, engineer • Magda VARGA, technician • Katalin Veresné-VÖRÖS, engineer • Tamás JÁSZI, engineer (left) • Sándor PÜSPÖKI, engineer (part time) • Zsuzsa PÜSPÖKI, engineer (part time) • Imre SZABÓ, engineer, dr. Univ. (part time) • Tamás SZABÓ, engineer (part time)
Ph.D. students / Diploma workers <ul style="list-style-type: none"> • Zsófia BAJI, Ph.D. student • Zoltán FEKETE, Ph.D. student • László GRAND, Ph.D. student • Tamás KÁRPÁTI, Ph.D. student • Endre LÁSZLÓ, Ph.D. student • Dorottya GUBÁN, M.Sc. diploma w. • Gergely MÁRTON, M.Sc. diploma w. • Péter NAGY, M.Sc. diploma w. • Tamás RETKES, M.Sc. diploma w. • Tamás WEIDISCH, M.Sc. diploma w. 	

The main task of the Microtechnology Department is the research, development and system integration of physical, chemical/biochemical sensors and systems:

- MEMS and MEMS related technologies, with special emphasis on development of Si MOS embedding circuits;
- Development and functional testing of different MEMS gas, chemical, 3D force, thermal, biology related sensors and sensor systems;
- Development of microfluidic systems;
- Development and applications of near IR light emitting diodes and detectors;
- Development of solar cells and their competitive technology.

Fundamental research on:

- sensing principles;
- novel materials and nanostructures;
- novel 3D fabrication techniques;
- ion-solid interaction for supporting MEMS development.

Device and material characterizations widely used in our projects:

- Ion beam analysis methods;
- IR and Raman scattering;
- Scanning Microprobes;
- Optical and Electron Microscopy, SEM, TEM, EDX;
- Spectroscopic Ellipsometry;
- Electrical characterisations.

The Microtechnology Department of MFA runs the 300 sqm clean lab (Class 100-10000) with the complete Si-CMOS technology together with a mask shop, unique in Hungary. A rather new and developing large facility of the Department is the CIGS solar cell technology laboratory equipped with a pilot line of sputtering, evaporation and laser scribing modules for 30×30 cm² glass substrates.

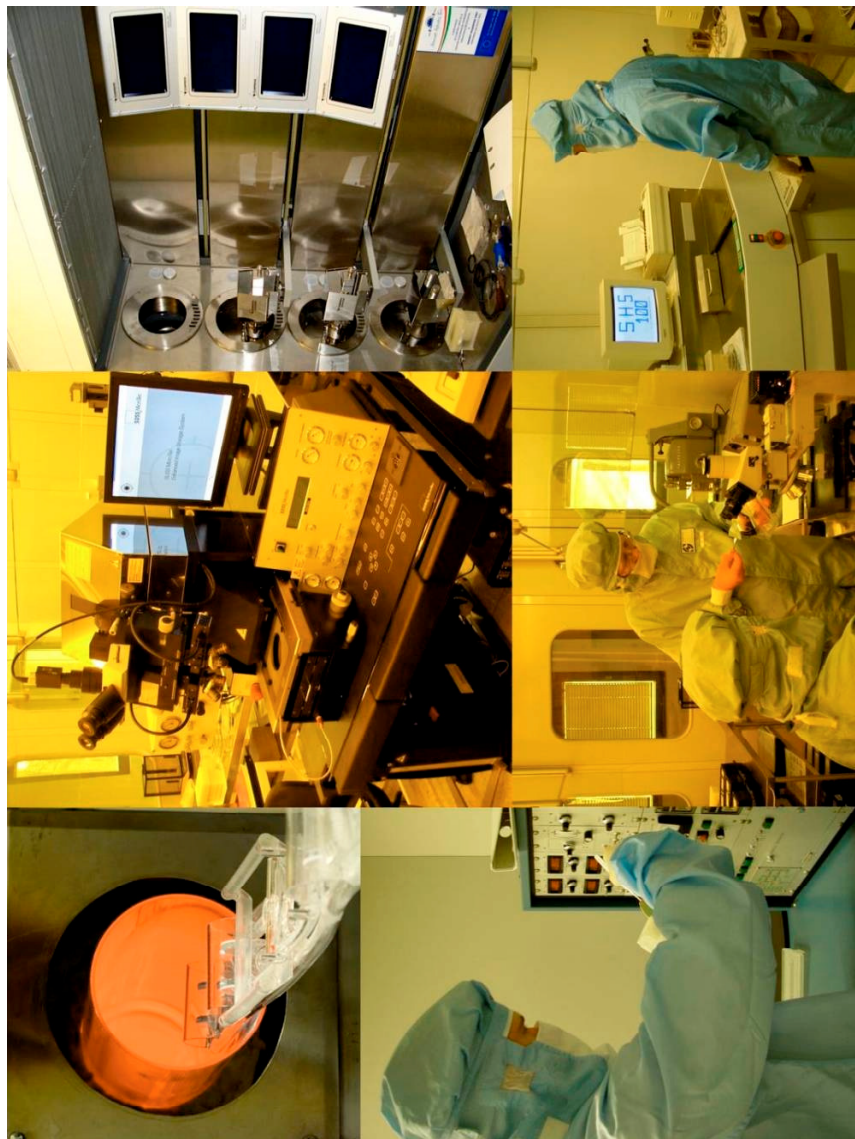
The technology base of the clean lab has been further improved in the recent years. A basic new technology – DRIE– was installed in 2010 into our Si technology line: Oxford Instruments Plasmalab 100 type deep reactive ion etching system was introduced in order to facilitate the works on 3D Si based MEMS devices.

Main technologies available in the Microtechnology lab for our partners and customers:

- High temperature annealing, diffusion and oxidation
- Rapid Thermal Treatment
- Low Pressure Chemical Vapor Deposition of poly-Si, SiO₂ and Si₃N₄ layers
- Low Temperature Chemical Vapor Deposition
- Ion implantation
- Thin film depositions – Electron beam evaporation, DC and RF Sputtering
- Atomic Layer Deposition
- Deep Reactive Ion Etching

- Photolithography with back-side alignment and Nanoimprinting
- Wafer Bonding
- Wet chemical treatments
- Electro-chemical porous Silicon formation
- Mask design, Pattern generator and Step-and-Repeat Camera
- Electrical and functional characterizations

Overview of the MFA Microtechnology clean lab



The recently installed Oxford Plasmalab 100 DRIE system



The load-lock and computer control of Oxford Plasmalab 100 DRIE system



Sensitivity tuning of a three-axial force sensor (ENIAC SE2A)

D. Molnár, A. Pongrácz, M. Ádám, Z. Hajnal, V. Timár-Horváth, A. Nagy, and
G. Battistig

In the frame of ENIAC SE2A project a Si mono-block, full-membrane, and three-axial force sensor is developed and optimized. In the Si element, a column like rod at the centre of a deforming membrane protrudes over the top surface of the device. Piezoresistors placed on the backside of the membrane, provide the signals for resolving the vector components of the load. The mono-block Si structure guarantees the perfect transmission of the attacking force to the sensing elements. The developed fabrication technology allows us to tune the sensitivity of the sensor easily by adjusting two lithographic steps defining the geometry of the sensor.

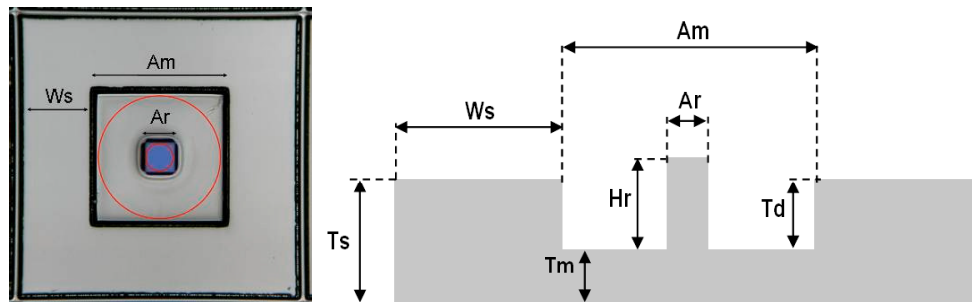


Figure 1 Top and cross sectional schematic view of the simulated and realized sensors. Membrane with square shape and its circular equivalent is marked by dotted and continuous lines, respectively.

Effect of membrane thickness, shape of the membrane and fill factor (the area of the rod/area of the membrane) on the sensitivity of the sensor is analyzed systematically by finite element methods using the COMSOL Multiphysics 3.5 software package.

Sensitivity of a resistor was analyzed as a function of membrane thickness (50-230 μm) while applying 1N normal and 45° shear force load. The sensitivity decreases with increasing the membrane thickness, as the resistivity change is inversely proportional to the square of the membrane thickness. It means that just by varying the thickness of the membrane, we could tune the sensitivity of a chip by one order of magnitude. Another important conclusion is that the square shaped sensors are more sensitive, than their circle shaped equivalents.

Based on the simulation results new layouts were designed and force sensor elements were realized. Experimental results were compared to simulations and good agreement was found.

Comparison of the characteristics of the different sensor designs obtained from simulations and from experimental measurements is also presented.

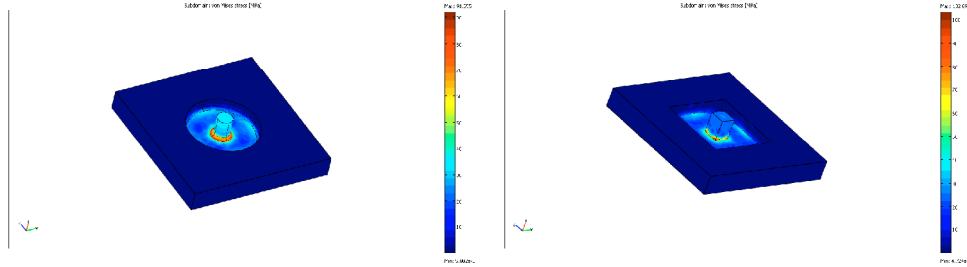


Figure 2 Overview of the equivalent stress on the circular (left) and square shaped (right) sensors to the resistance change

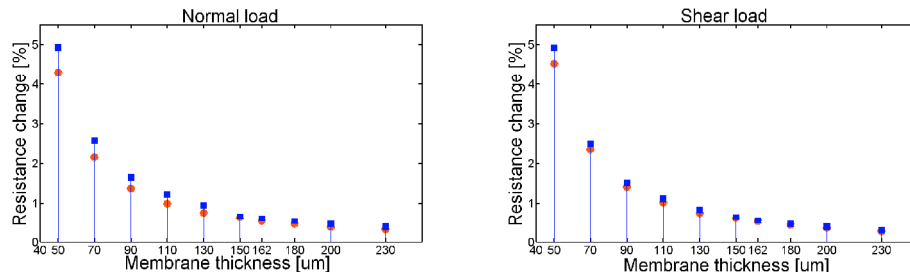


Figure 3 Relative resistance change versus membrane thickness for 1N normal (left) and shear (right) load on square shaped (marked with blue squares) and circular (marked with red circles) sensors

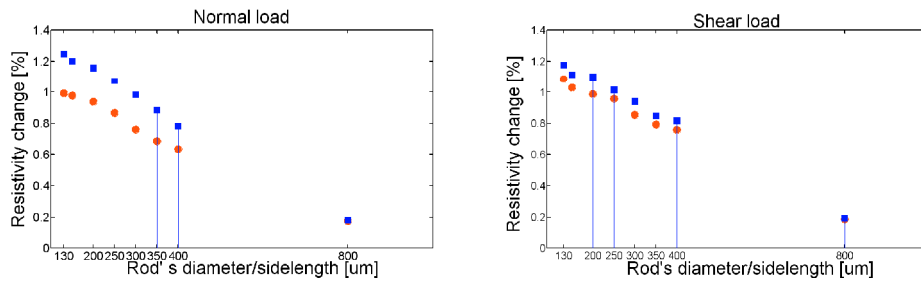


Figure 4 Relative resistance change versus fill factor for 1N normal (left) and shear (right) load on square shaped (marked with blue squares) and circular (marked with red circles) sensors

The experimental setup consisted of a loading instrument, signal measuring system and data processing. Piezoresistors with their reference pairs were arranged in a half-bridge configuration to provide a direct voltage reading proportional to the strain. Responses to the normal loading in all four elements are approximately equal, since the stress and the arising strain at the position of all the symmetrically arranged piezoresistors in the membrane is similar.

Sensors realized with the following parameters were tested using Andilog Centor force gauge: side length of the membrane is $940\text{ }\mu\text{m}$, side length of the transmitting rod is $200\text{ }\mu\text{m}$, thickness of the membrane is $162\text{ }\mu\text{m}$, and height of the rod is $310\text{ }\mu\text{m}$. In response to normal loading, the sensor outputs were recorded at different force magnitudes in the 0-2.5 N range.

As expected the input-output characteristics was linear and resulted in a sensitivity of 5.98 mV/V/N . Note, the calculated value is 6.01 mV/V/N , for a sensor with $162\text{ }\mu\text{m}$ thick square shaped membrane, which is in good agreement with the measurements. Sensitivity tuning of a full membrane mono-block 3D force sensor was shown by varying geometrical parameters of the structure. Finite element simulations show that sensitivity depends on the membrane thickness, the shape of the membrane and the ratio of the transmitting rod/membrane area, too. Calculated sensitivity forecasted by FE analysis was compared with experiments on realized sensors.

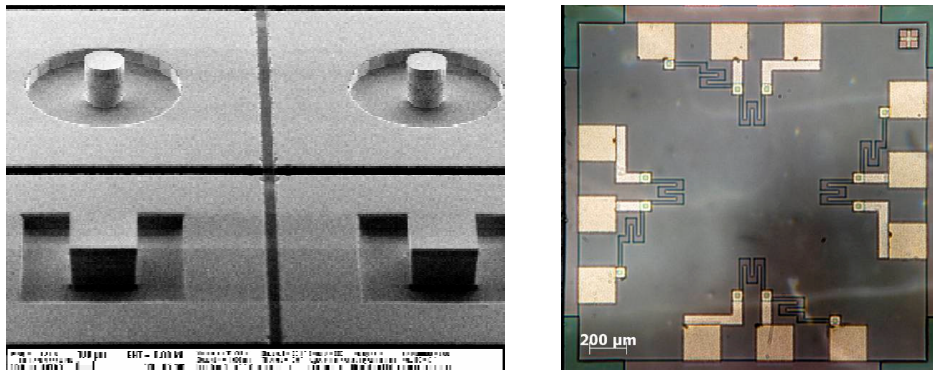


Figure 5 Front (left) and back-side (right) images of the fabricated sensors.



Figure 6 The measurement set-up with the force gauge and the chip

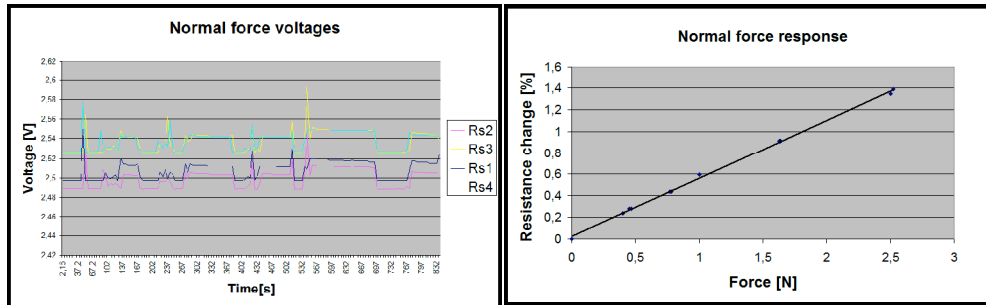


Figure 7 Voltage response of the resistors to normal loadings versus time. b) The linear input–output characteristics of the sensor with square shaped 162 μm thick membrane and rod with side length of 200 μm

Thermal behaviour of 3-dimensional single crystalline force sensor (ENIAC SE2A)

G. Battistig, T. Weidisch, T. Retkes, M. Ádám, I. Bársony, A. Nagy, and T. Mohácsy

A piezoresistive-type integrable single-crystalline sensor was developed for 3D force sensing. The piezoresistance effect is inherently temperature-dependent; therefore thermal properties of the device were studied. Furthermore, the elastic cover and the packaging strongly affect the thermal behaviour of the sensor. The temperature dependence of the offset and the sensitivity were measured and the value of temperature coefficient of offset and sensitivity were calculated. In sensitivity we found a nonlinear relationship and a remarkable drop over the temperature of 45 °C. There are less demanding applications, where - in spite of their temperature sensitivity - the force sensors are appropriate, however, for precise tasks temperature compensation is indispensable. On this reason a new perforated membrane force sensor design was proposed and manufactured, providing the necessary signals for obtaining temperature compensated outputs.

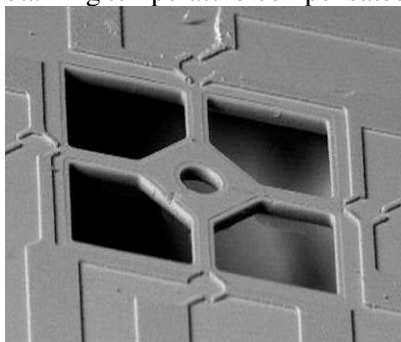


Figure 1 Previous design: SEM micrograph of the bare sensor (on the left) and the mounted and covered chip (on the right).

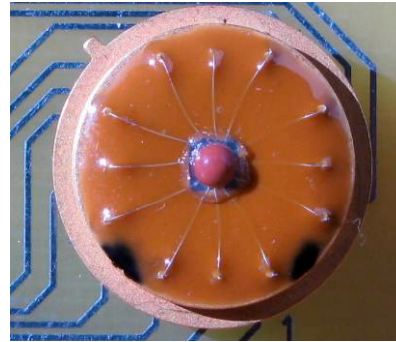
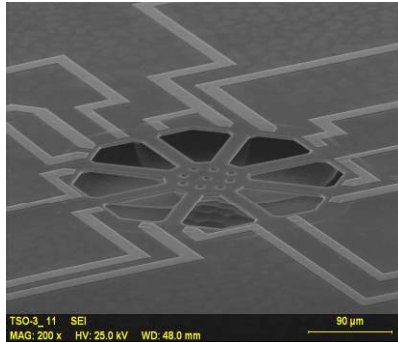
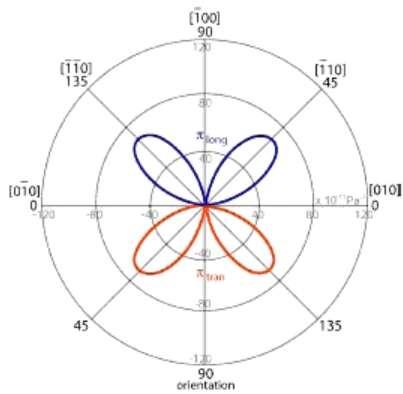
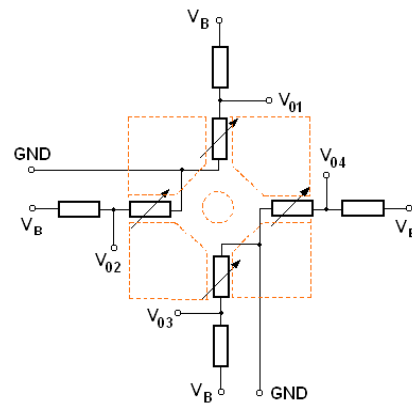


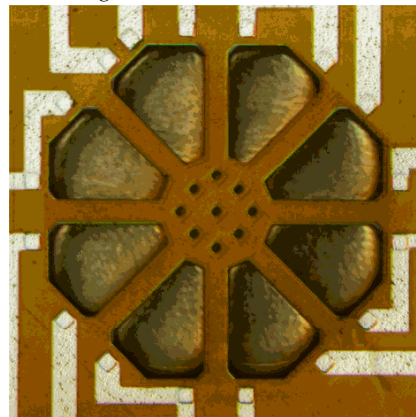
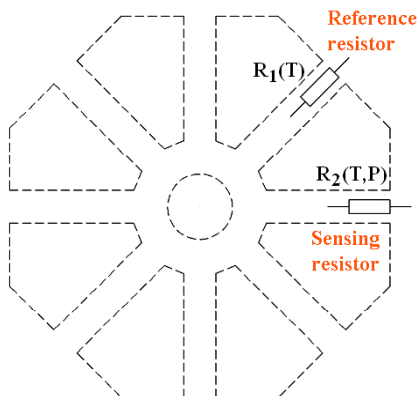
Figure 2 New design: for thermal compensation.



Strong orientation dependence of piezoresistivity in silicon



Scheme of a piezoresistive-type 3D force sensing element



Schematic top view and optical microscope image of the proposed and manufactured new 3D force sensor design.

Figure 3

Temperature sensitivity is a major concern for piezoresistive sensors. To eliminate the effects originating from different thermal boundary conditions in the reference and sensor elements, a new structure was proposed. The reference resistors are aligned to [100] or equivalent directions and they remain insensitive to mechanical stress. Therefore, they can be formed in thin bridges, where they operate at identical thermal conditions with the sensor elements on the same perforated membrane.

As our measurements show the Non-covered chips have a positive, while the elastic rubber covered ones a negative offset warm-up shift. Up to 5V bias the rate of change is nearly equal for both sensor types.

The reason for the thermal response in bare sensors is based on the temperature difference of the sensing and reference resistors. Reference resistors are placed in the heat-sinking bulk Si, while the sensing resistors lie on the thermally more isolated membrane so thus they are exposed to different thermal conditions.

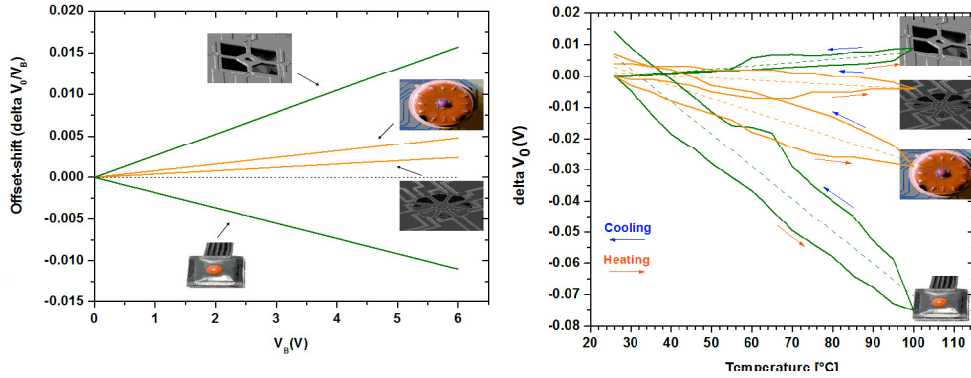


Figure 4 Offset-shifts of bare and covered sensors (left) vs. power supply and (right) vs. ambient temperature.

In order to calculate the thermally independent pressure sensitive component of the sensor element, the continuous measurement of the voltages $V_1(T)$ and $V_2(T,P)$, and the storage of $V_1(T_0)$ and $I(T_0)$ – both measured at T_0 – is required.

$$R_2(T_0, P) = \frac{V_2(T, P)}{V_1(T)} \frac{V_1(T_0)}{I(T_0)}$$

A thermally compensated bulk micromachined 3D force sensor is developed. A novel approach is proposed based on the utilization of the anisotropic piezo-sensitivity in silicon, appropriate for realization by perforated thin Si membrane technology.

Separation of biological samples in microscale

(Projects EU FP7 P3SENS, ENIAC JTI, CAJAL4EU project via the National Office for Research and Technology)

Z. Fekete, P. Nagy, and P. Fürjes

Demands for analytical devices applicable for in situ diagnostics far from clinical environment using small sample volumes and not requiring professional staff is apparently increasing in the clinical practice. Such requirements can be fulfilled by microfluidic systems. This miniaturization effort enables, for example, the acceleration of low-cost clinical tests by largely decreasing sample amount needed for a single test and realizing High-Throughput (HT) quick and cost effective analytical systems.

One of the first preparation steps of blood sample tests is the separation of the blood plasma from whole blood, since the detection of specific blood markers in the blood plasma may prove the presence of several cardiovascular diseases. To establish fast diagnosis, the realization of that function in today's microfluidic systems is therefore essential. Special microfluidic structures can be applied for hydrodynamic focusing and positioning the solution in the microchannels, or for inertial separation of dissolved particles by size. Utilizing the Zweifach-Fung effect the highly polarised blood cells can be transported separately from the plasma.

Our group aimed the investigation of the Zweifach-Fung separation phenomenon. In order to analyse the geometric effects and biomechanics of red blood cell flow, special microstructures (see Figure 1) were fabricated in single-crystalline silicon by Deep Reactive Ion Etching (DRIE). The sealing cap and connections of the fluidic system was realized by a Nd:YAG laser in Pyrex glass. The leak-free alignment of the substrates was carried out by anodic bonding.

The results of the promising measurements, directed to the determination of the efficiency and quality of the above mentioned separation technique, are being evaluated.

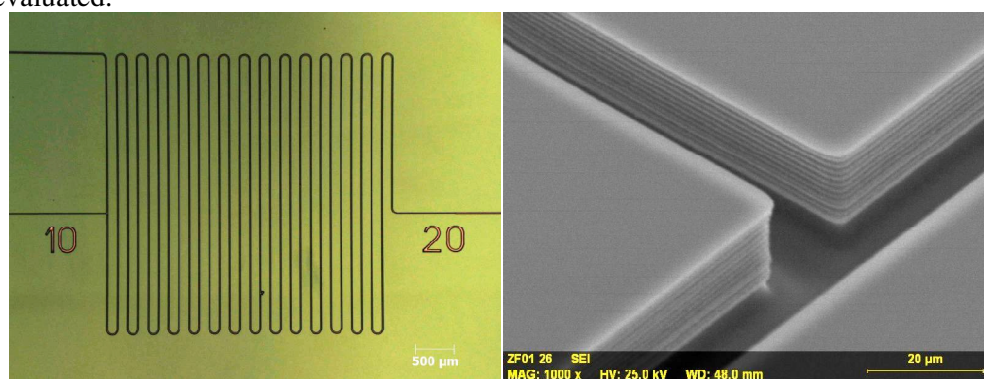


Figure 1 Representative silicon test structure for Zweifach-Fung plasma filtering fabricated by DRIE.

Sample transport in polymer based microfluidic system

(EU FP7 P3SENS project)

P. Fürjes, Z. Fekete, E. Tóth, and E. Holczer

Manipulation of fluids (e.g. biological samples) in analytical systems is a key issue in terms of the final applicability of these devices. In novel analytical microsystems the sample manipulation is executed by complex micro-fluidic structures, which can perform the main sample preparation tasks such as mixing, dilution, transportation, and separation; all of these complex tasks realized in a single integrated structure. Complex fluidic devices integrating active and passive micro-systems, as well as combining silicon micromechanics and polymer technology can be applied for fast, low cost and intelligent sample control at the microscopic scale.

The basic function of the fluidic structure is the transportation of the diluted sample from the inlets to the sensing area of the device. Another important function of the fluidic structure is the dilution and complete mixing of blood sample with an adequate buffer solution. Several possible mixing strategies can be found in macroscale as molecular diffusion, turbulent diffusion, advection and Taylor-dispersion. Due to the small dimensions of the microfluidic systems usually the flows are laminar and the component streams mix only by diffusion, creating a dynamic diffusive interface with predictable geometry. The advection generated by the fluid flow which results in a chaotic distribution of the molecules, could be an ideal mixing method in the case of microfluidics considering stable and laminar flow.

The mixing behaviour of the microfluidic structures was analysed by numerical modelling to determine the mixing efficiencies. For reference a simple T-mixer structure was implemented with rectangular cross-section. In addition, an advanced T-mixer staggered by blocks and a Herringbone type chaotic mixer structure were also investigated.

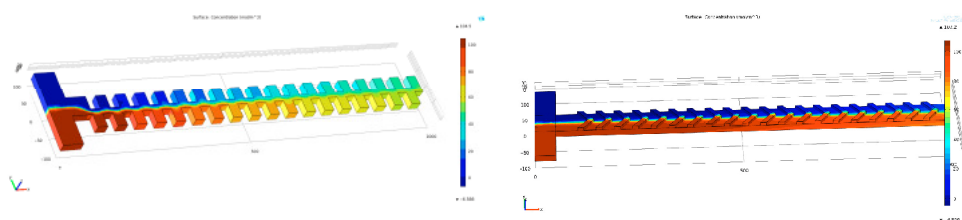


Figure 1 Representative concentration distribution in staggered blocks T-mixer and Herringbone mixer structure.

When micro-fluidic structures transport biological samples (like blood, serum, saliva, etc.) the material selection and the determination and control of surface effects taking place on the channel walls have crucial importance. Beyond the conventional materials applied in micromechanics like silicon and glass low cost polymer based systems gain increasing interest. The wetting effects of these materials have significant influence on the behavior of the flow. Moreover, from biological samples

the non-specific binding of proteins or other molecules on the channel surfaces is also critical and can influence the analytical results affecting the final applicability of the system. All of these effects have to be carefully considered and investigated in detail in order to find the most suitable materials for a given application.

Among the polymer materials the most attractive candidates to realize simple microfluidic systems are Polydimethylsiloxane (PDMS) and the epoxy-based negative photoresist*. These materials are relatively cheap (especially PDMS) and can be easily microstructured using standard photolithographic processes (with resolution of 1 μm at MFA). PDMS is also well suited for mass production, since it can be replicated from photoresist microstructures serving as replication masters. Using the above mentioned processes microfluidic channels in the thickness range of 5-100 μm can be fabricated at MFA. To form the microfluidics in different polymer materials (SU-8 and PDMS) two variations of the realization processes were developed. Both of them apply the described multilayer SU-8 technology to form the moulding form for PDMS or directly the microfluidic structure.

The transport fluidic systems subscribed further – containing 3 different mixer components – were realized in both PDMS and SU-8 polymer materials. The realized structures are presented in Fig. 2.

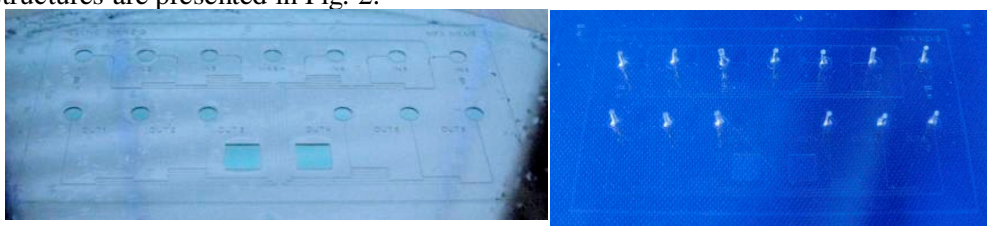


Figure 2 The microfluidic layouts realised in SU-8 (left) and PDMS (right) polymers.

The permeability and sealing of the fluidic channels are adequate although the pressure sustainability and washing and mixing efficiencies in case of the different mixer structure are to be evaluated. Fig. 3 represents the applicability of the realized structure containing the parallel channels.



Figure 3 Fluid flow in the 6 parallel channels over the sensing area of the optical structure.

*SU-8, MicroChem Corp.:

http://www.microchem.com/products/su_eight.htm

Chemically Modified Solid-State Nanopores for Sensing

(ENIAC JTI, CAJAL4EU via the National Office for Research and Technology, OTKA No. NF69262)

P. Fürjes, A. L. Tóth, and R. E. Gyurcsányi

Sensing with chemically-modified nanopores is an emerging field that is expected to have major impact on bioanalysis and fundamental understanding of chemical interactions on nanoscale down to the single-molecule level. The main strength of nanopore sensing [R. E. Gyurcsányi, *Trac-Trends In Anal. Chem.* 27 627-639 (2008)] is that it implies the prospect of label-free single-molecule detection by taking advantage of the built-in transport-modulation-based amplification mechanism. Here we present the development of nanopore based sensors, including methodologies for fabrication of single- and multichannel nanopores in solid-state membranes with diameters ranging from 5 to 100 nm, their chemical modification and application for bio(chemical) sensing (Fig. 1).

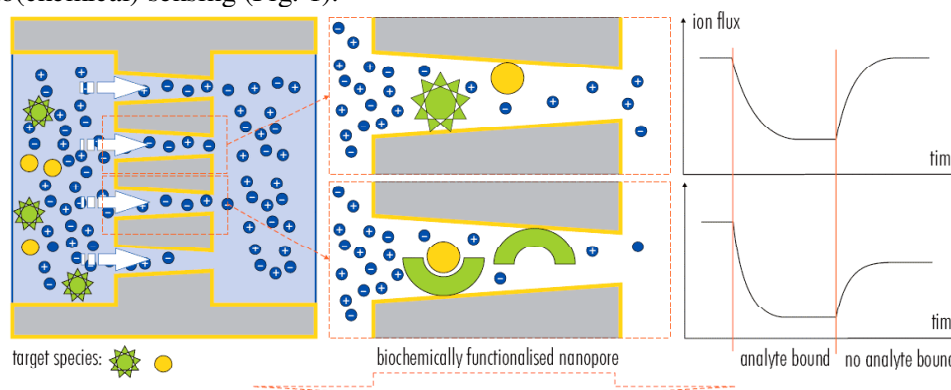


Figure 1 Application of the nanopores for sensing

Solid-state single gold nanopore structures were fabricated by the combination of the silicon based 3D MEMS/NEMS technology, and special subsequent nanofabrication techniques, such as subtractive nanoscale modification of the existing microstructure by focused ion beam etching. (Fig. 2.a) **Multichannel gold impregnated nanopore membranes** (Fig. 2.b) were also fabricated and characterized. For interfacing the nanopore membranes a special crossing microchannel structure was designed combining the silicon 3D micromachining with both SU-8 and PDMS polymer structuring.

In order to use nanopores as selective detectors, their surfaces must be chemically modified. The functionalization of the nanochannels passing through the gold layer and the method of transport-modulation-based selective molecule detection were developed by the Research Group for Technical Analytical Chemistry of the Hungarian Academy of Sciences at Budapest University of Technology and Economics.

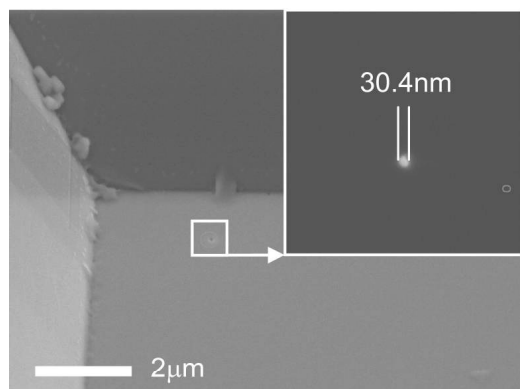


Figure 2a Single nanopore in solid-membrane.

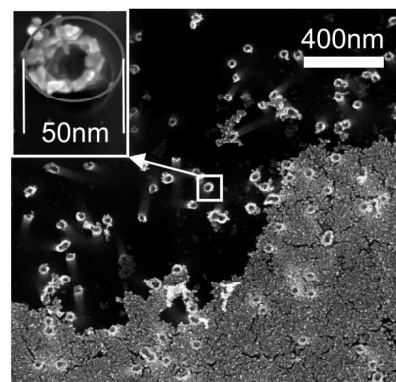


Figure 2b Multichannel nanopore membrane

The capabilities of nanopore based sensors in terms of detection limit are explored by using random walk simulation and multiphysics modeling. Apparently, the detection limit of single nanopore based affinity sensor is determined by the probability of a successful encounter between the nanosensor and analyzer. Since in principle even a single molecule can be detected by nanopore sensors, the detection limit of such sensors was also explored in terms of concentration. However, significant improvements are obtained upon directing the analyte into the sensing zone of the nanopore by means of an electric-field or pressure gradient.

Besides introducing specific receptors chemical modification can be also used to protect surfaces from biofouling, or to induce specific transport modulation effects. Aspects of thiol (dithiolan, disulfide) chemistries for building up self-assembled molecular architectures with molecular recognition capabilities (Fig. 3) are demonstrated [50].

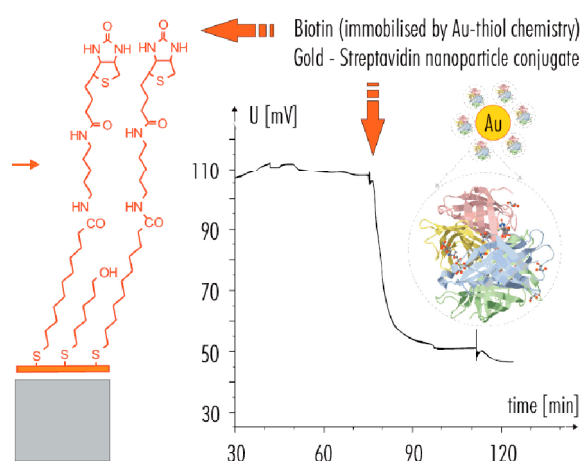


Figure 3 Selective molecule recognition by a chemically modified gold nanopore

Investigation of silicon-based superhydrophobic surfaces

(EU FP7 P3SENS project)

P. Fürjes, Z. Fekete, and T. Pardy

Recently there was a significant progress in the development of water-repellent surfaces regarding biomimetics or ElectroWetting on Dielectric (EWOD) for digital microfluidics. Bioinspired surface topographies are of key importance, therefore a range of micromachining concepts have been demonstrated. The fabrication of superhydrophobic surfaces has involved a wide variety of techniques including surface preparation, micromachining and the application of several surfactants. In spite of the rapid development of dry etching techniques, like deep reactive ion etching (DRIE), there is still room for further investigation as regards the combination of less expensive wet etching techniques.

The functionality of the micro- or nanofluidic structures is significantly influenced by the surface properties of the applied structural materials. The fluidic behaviour can be modified by micro- and nanoscale surface structuring and deposition of additional coatings. In our work, the effects of 3D surface topography, nanoscale roughness and additive chemical layers were discussed.

MEMS compatible processes, as two-step wet chemical etching and Deep Reactive Ion Etching was elaborated and characterised for modification of surface properties of silicon combined with subsequently deposited dielectric layers (Hexamethyl-disilazane - HMDS or plasma-polymerised fluorocarbon). The feasibility of the combined technique was demonstrated by the analysis of the wetting behaviour of the realised structures applying contact angle measurements. The developed micro- and nanoscale surface topographies by wet and dry etching techniques was also characterised by AFM and SEM.

In our laboratory, a two-component alkaline etching (NaOH , NaOCl) in case of different substrate orientation and subsequent polishing ($\text{HF}:\text{HNO}_3:\text{H}_3\text{PO}_4$) with varied mol-ratio was investigated. The proposed alkaline etching was successfully applicable for the formation of high aspect ratio microstructures, see Figs. 1(a) and (b). To evaluate the feasibility of the technique microstructures of similar patterns were also produced by DRIE (Fig. 1(c)).

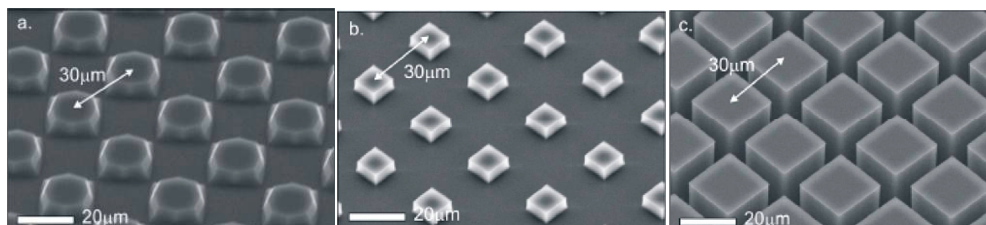


Figure 1 3D silicon microstructure array formed by two component alkaline etching (a, b) and deep reactive ion etching (c.)

The combination of the 3D bulk micromachining and the subsequent chemical layer deposition steps is expected to modify the surface behaviour of the silicon radically. The microstructured silicon surfaces coated by plasma-polymerised poly-fluoro-carbon represented excellent hydrophobicity (see Fig. 2).

Contact angle measurements in case of the different structures (geometric parameters are listed in Table I) coated by poly-fluoro-carbon deposited by DRIE proved the feasibility of the fabrication process. Results for two-component alkaline etching solution (at the orientation of 45°) are illustrated in Fig. 3.

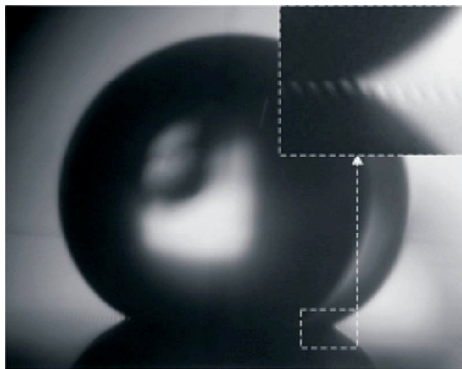


Figure 2 Superhydrophobic behaviour demonstrated on solid-air composite surface fabricated by two-component alkaline etching and subsequent plasma-polymerisation of poly-fluoro-carbon layer. Air cushions are clearly shown in the enlarged area.

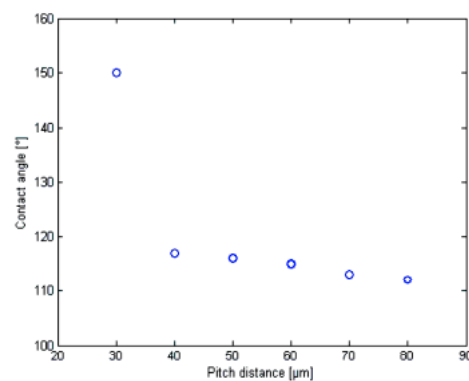


Figure 3 Measured contact angles at different pitch distances in case of chips fabricated by alkaline etching. Cassie-Wenzel transition is apparently noticeable on the figure.

Z. Fekete, A. Pongrácz, and Á. Szendrey

The production technology of buried channels is based on Deep Reactive Ion Etching (DRIE). The subsequent using of Bosch process, anisotropic oxide and isotropic silicon etching recipes results in microchannels well below the wafer's surface (Fig. 2). By the deposition of LPCVD poly-silicon sealed channels are created which can be used as part of injection systems in microcantilevers used as i.e. cerebral probes. The technological parameters of the process are still being tuned, and the effects of the plasma etching mechanisms are investigated in order to establish design rules.

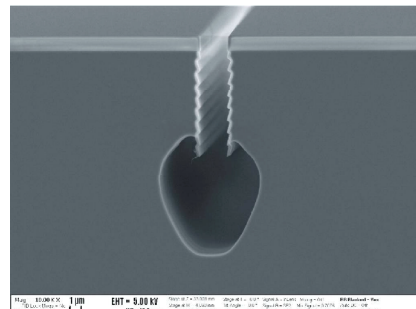


Figure 2 „Almost buried” microchannel in silicon before the last step of LPCVD poly-Si deposition

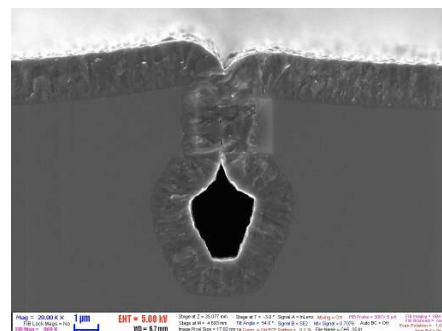


Figure 3 Buried microchannel after the SiO_2 removal and LPCVD poly-Si deposition.

Development of THz detectors

(OTKA No 77843, 77997, and 73424 NK)

B. Szentpáli, P. Fürjes, E. László, P. Basa, G. Battistig, I. Bársony,
G. Károlyi (BME), and T. Bercei (BME)

Recently THz and mm wave radiations find widespread application, albeit their management is more difficult than that of microwaves. A serious bottleneck is the lack of choice of appropriate detectors. Even the best microwave Schottky diodes have their cut-off frequency within these bands. Micromachined thermopiles are widely exploited for measuring the intensity of the infrared radiation, etc. A novel MEMS thermopile structure is proposed, which consist of linearly arranged p- and n-type polysilicon strips instead of the conventional loop-like configuration [129]. The traditional thermopile and the novel structure are shown in Fig. 1 (a) and (b).

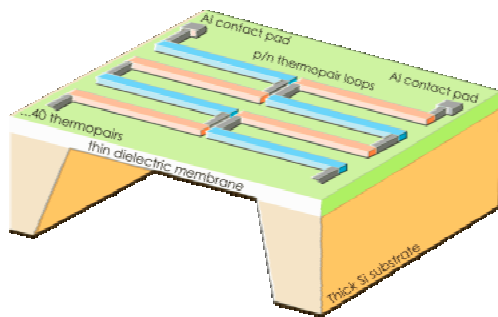


Figure 1 (a) The outline of a MEMS thermopile for measuring the infrared radiation. The good heat isolation on the membrane makes possible the formation of temperature difference between the hot and cold ends of the thermocouples.

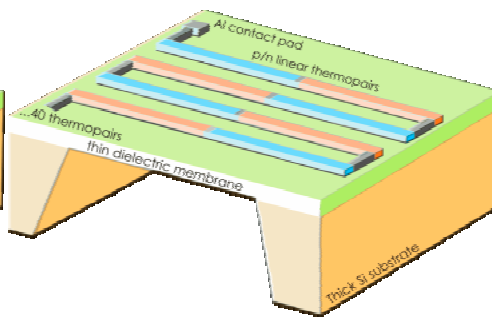


Figure 1 (b) The proposed linear arrangement of the thermopairs. Here the thermocouple lines act as short circuited dipole antennas, in which the distribution of the induced current is sinusoidal, having the maximum value at the centre. Therefore the heat formation peaks around the middle of the lines, exactly where it generates the highest thermoelectric effect.

The conventional poly-silicon thermopile technology was combined and improved by double side bulk silicon micromachining for the realization of the designed structure [131], [M. Graf et al, Meas. Sci. Technol. 18 R59-R75 (2007)], [H. Seidel et al, J. Electrochem. Soc. 137 3612-3638 (1990)]. Towards reducing the residual stress of the suspended membrane a stacked layer structure was applied containing non-stoichiometric silicon-nitride (SiN_x) and silicon-oxide (SiO_2) as structural materials with adequate thickness ratio. The sheet resistivities of the n and p type poly-silicon were $23.7\Omega/\square$ and $37\Omega/\square$, respectively.

Four types of measurements were performed on the devices. The responsivity against direct heating was investigated on loop-like structures with the integrated heater placed between the hot ends of the loops. The thermal coefficient of the heater resistance was obtained from independent measurement, and using this value the temperature of the heated resistor was calculated. On this way the thermopower was determined to be 18 mV/K for the 40 p-n pairs, while the responsivity was found to be 90 V/W. The responsivity to infrared radiation was measured with the help of a black body heated gradually up to 100 °C. There is no information about the reflected and transmitted power; the responsivity was calculated as the total black-body radiation impinging the sensor, which was not covered by any absorbing medium. No significant difference was observed between the behavior of the linear and the loop-like structures.

The responsivities in the microwave and millimeter wave bands were measured in the K_u-band, at 13 GHz and in the W-band at 100 GHz. In the K_u-band the radiation emitted by the open end of the rectangular waveguide was used, while at W-band the beam was expanded by a small horn antenna. In these experiments there was no any information on the reflected and transmitted signal and the responsivities were calculated from the full power. The polarity dependence was very significant at both frequencies. The maximum of the output was obtained when the *E* field was parallel to the lines and it falls to the level of the background noise in the orthogonal case. The loop-like structures did not produce any significant output over the background. Table I summarizes the measured responsivities.

Method	Responsivity [V/W]
electrical heating	90
thermal radiation	20
13 GHz	0.2
100 GHz	5.58
Table I	

It is obvious that electric heating results in the largest responsivity. In this case all the power is directly introduced into the thermopile, close to the hot point. The infrared radiation is absorbed only partly and it is uniformly distributed along the surface. The responsivity at 100 GHz is reasonably greater than at 13 GHz. This fact supports the antenna-like operation of the device; the 1.6 mm long antenna should have a resonance at around 100 GHz, while at 13 GHz it is a short dipole with low efficiency.

The measurements at 100 GHz were made at the Universität Duisburg-Essen, with the kind help of Vitaly Rymanov and Prof. Andreas Stöhr. Their contribution is acknowledged.

Deposition of Al doped ZnO layers by Atomic Layer Deposition

(OTKA NK 73424, TFSOLAR02)

Z. Baji, Z. Lábadi, Z. E. Horváth, M. Fried, B. Szentpáli, and I. Bársony

In the field of thin film solar applications there is a stringent need for limitation of thermal budget given by the substrate and the active layer alike. Recent advancement in polymer-based solar cells restrict the maximum applicable temperature to $< 250^\circ\text{C}$. A vacuum-compatible low temperature method for TCO ZnO deposition could be the use of Atomic Layer Deposition (ALD) especially when the requirements for conformality are substantial, as in the case of e.g. thin buffer layers. Setting the conductivity of this TCO or buffer layer is, however, not obvious, since the introduction of substitutional Al dopants into the ZnO matrix is a thermal budget influencing step as well.

Our work was aimed at the study of a combined deposition of a controlled level of Al content in ALD grown ZnO by using alternate precursor pulse method. The source of Al dopants in this case is the AlO_x interlayer. The ALD temperature window for Al_2O_3 is, however, around 300°C , above the optimum ZnO temperature window of around 170°C . We analysed the incorporation and activation of a controlled amount of Al around this optimum temperature of the ZnO ALD growth.

We examined both the effects of different Al contents and deposition temperature on the conductivity and structure of the layers, in a wider doping and temperature range.

Results:

- (i) specific resistivity of the layer as a function of Al content shows a minimum curve
- (ii) incorporation of Al into the layer is proven by EDS spectra
- (iii) even 0.1 at % Al decreases the specific resistivity
- (iv) XRD spectra of the samples show that Al incorporation changes the preferred orientation of the polycrystalline layer
- (v) layers with resistivity of $10^{-3} \Omega\text{cm}$ can be deposited at 150°C substrate temperature

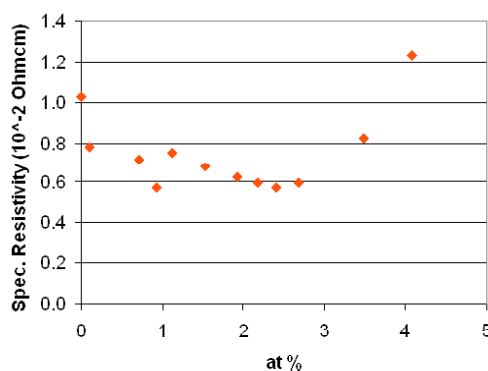


Figure 1 Specific resistivity vs. Al content of Al:ZnO layers deposited at 150°C

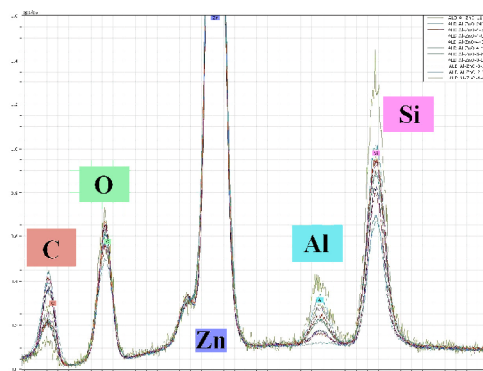


Figure 2 EDS spectra of the ALD Al:ZnO layers showing the Al incorporation

Growth of CIGS layers by post-selenization of metal precursors

(OTKA NK73424, TFSOLAR02)

Z. Baji, Z. Lábadí, G. Molnár, A. L. Tóth, and I. Bársony

The post-selenization of CuInGa metal precursor layers is a possible way to form CuInGaSe₂ active layers for solar cells, but it is relatively less developed and less extensively studied area. Our method to form CIGS layers is based on precursor evaporation from an alloy source (alloying takes place during the heating of the evaporation sources). Metal precursors were weighed in to provide CuIn_{0.8}Ga_{0.2}Se₂ compound. Evaporation of metals was made from Ta boat at 1500-2000 °C and the full load was evaporated from the boat. Metal precursors were subsequently selenized in sealed glass ampoules under Se vapour pressure at 500°C.

XRD spectra of the layers showed that the whole layer consisted of CuIn_{0.8}Ga_{0.2}Se₂ phase. Fig. 1 shows the morphology of the layer after 5 min post-selenization.

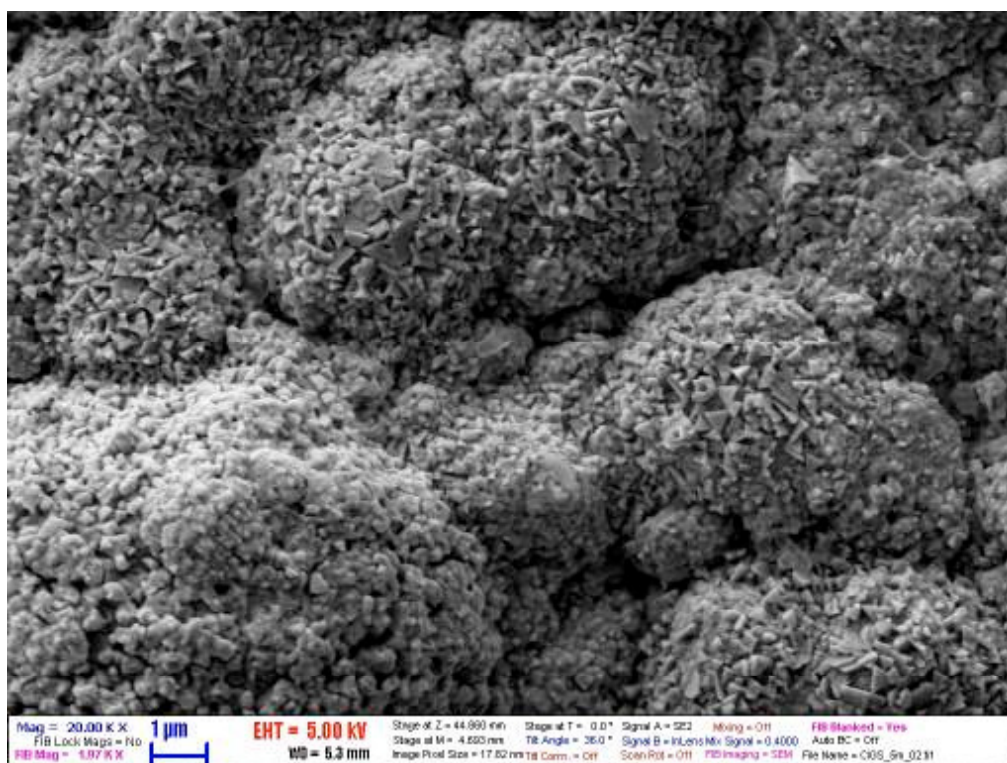


Figure 1 SEM morphology of a CIGS layer formed by 5 min post-selenization at 500 °C

Wafer bonding for microelectronics

T. Kárpáti, and A. E. Pap

The wafer bonding technology is of great importance in microelectronics (for example packaging) and micromachining. Wafer bonding refers to the mechanical fixation of two or more wafers to each other. It is of great account that the whole bonding process is compatible to microelectronics technology. The SüSS MicroTech SB6L Wafer Bonder at MTA MFA allows low temperature bonding (max. 500°C). Also, both electro-assisted and wafer bonding by thermocompression is possible. We can bond several kinds of materials and wafers of various sizes (max. 4”), see Table I. Some of our results for wafer bonding are shown in Figs. 1-3.

Materials		Type of wafer bonding		Details
Type A	Type B	Thermocompression	Anodic	Bonding strength
Si	Si	+		Strong
Si	Glass*		+	very strong
Si + SiO ₂	Glass*		+	strong
Si + SiN _x	Glass*		+	weak
Glass*	Glass*	+		strong
Glass**	Glass**	+		strong
Glass* + dep. Si	Glass*		+	very strong
SiN _x	SiN _x	+		weak
Al	SiN _x	+		weak
Al	Al	+		weak

Glass* - Schott Borofloat® 33; Glass** - quartz glass

Table I Different materials and their nature of bonding.

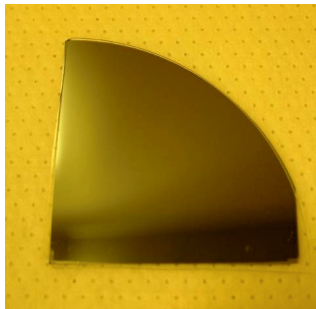


Figure 1 Si and Borofloat® 33 anodic bond

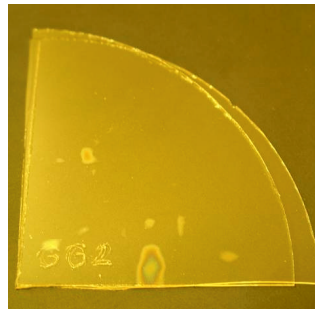


Figure 2 Glass to glass thermocompression bond



Figure 3 Glass to glass anodic bond with deposited Si intermediate layer

The great advantage of wafer bonding is its flexibility and wide range applicability in the development of different MEMS structures. It could form simple hermetically closed cavities or create mechanically fix substrates for chips. By means of bonding it is easy to develop microfluidic devices with structured wafers. Another application is to create back side electrical contacts for sensors, see Figs. 4-5. In addition, Fig. 6 shows how a closed pressure of 500 mbar can unsharpen a thick Si membrane.

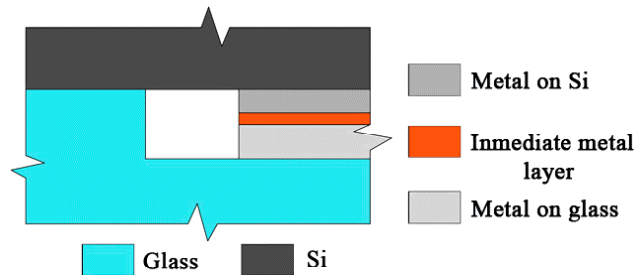


Figure 4 Schematic draw of electrical contacts and mechanical fixation between two wafers

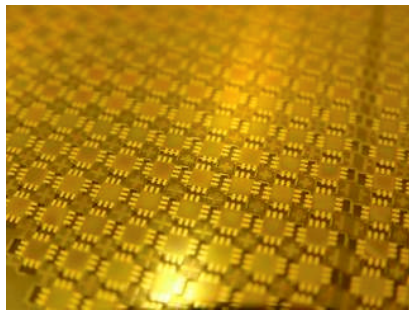


Figure 5 Electrical contacts between two wafers.

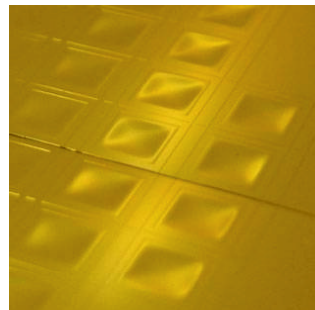


Figure 6 A pressure of 500 mbar closed in a cavity

One of our completed projects with wafer bonding technology is the silicon based capacitance pressure sensor. The device can measure in the 0-1000 mbar pressure range. The geometrical size of the sensor is 5 mm × 6 mm with 1 mm thickness. The integrated membrane thickness is 10 μm and the sensing area is 11.56 mm², see Fig. 7). Fig. 8 shows measurements performed with capacitive pressure sensors.

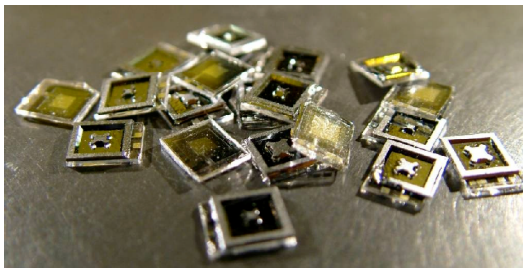


Figure 7 MEMS capacitive pressure sensors.

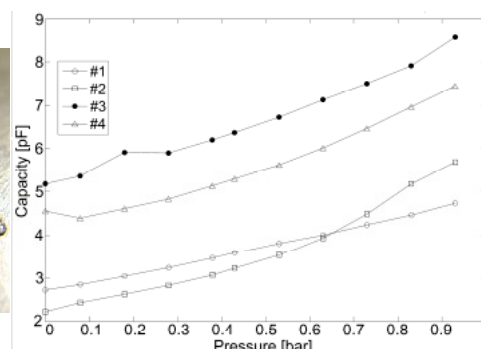


Figure 8 Measurements performed with MEMS capacitive pressure sensors.

MBE related research and development in MFA

(OMFB-01109/2009, OTKA K75735, OTKA K77331)

Á. Nemcsics, I. Réti, G. Tényi, P. Kucsera, P. Harmat, L. Tóth, R. Hodován,
Á. Szendrey, B. Pődör, J. Balázs, L. Dobos, and J. Makai

The main part of our MBE equipment is originated from a donation, which was a consequence of a long time scientific cooperation led by Á. Nemcsics. The MBE Laboratory (Joint Research Laboratory of MTA-MFA and ÓE-MTI) shared between our Research Institute and the Óbuda University, Institute for Microelectronics and Technology was inaugurated in 2009 November [Á. Nemcsics *et al*, *El. Tech. Mikrotech.* 48 33-35 (2009)]. Our MBE equipment has three UHV chambers such as a reactor-, a supplement-, and a load-lock chamber. The reactor chamber is equipped with 4 effusion cells (Ga, As, In, Al). The sample holder is mounted on a precision manipulator. The electron beam sample heating arrangement provides a quickly changeable temperature control, which is important at the production of multi quantum well structures. A 10 kV RHEED is provided for in-situ monitoring of the process. A sample chamber is joined to the main chamber with a vacuum shut-off valve where the manipulation of the sample is facilitated by magnetic rods. The RHEED picture can be viewed on a fluorescent screen opposite of the electron gun. Since the fluorescent screen is not suitable for the accurate measurement of the intensity change, a Faraday-cup, mounted on a precision manipulator, measures the electron current directly, which is the speciality of our equipment. A turbo pump and an ion-getter pump provide for the evacuation of the two chambers. The load-lock chamber with the manipulator and with four sample containers is our own development [90]. Furthermore, the equipment was supplied by PLC controlled heatings and shutter moving and also by RHEED evaluation with image processing [72, 89].



Figure 1 View of our MBE equipment.

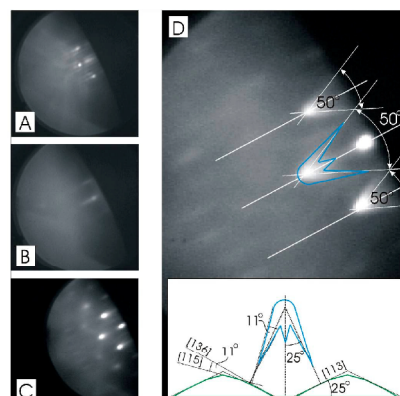


Figure 2 The change of the RHEED pattern during the QD formation

Investigation of MBE grown quantum structures.

Recently, the growth of self-assembled quantum structures has been intensively investigated for basic physics and device applications. It is very important to understand their growth process and to know their particular shape. The archetypal system of these nano structures is the lattice-mismatched system, where the strain-induced process leads to the formation of QDs. The detailed electronic structure of a QD, which governs electronic and optical properties, depends on its shape. It is generally agreed that the essential driving force for coherent lattice mismatched QD formation is strain relaxation. In this field, the self-assembled lattice matched quantum structures employing droplet epitaxy is an interesting and novel alternative against the established technology of strain-driven QD formation. With this method, we can prepare not only QDs but quantum rings (QRs) and other various quantum structures. Today, a theoretical description is not yet available for the underlying growth mechanism, i.e. the development of faceting in the case of droplet epitaxy even so it is very important to understand the growth kinetics. We have given explanation of the RHEED pattern for different quantum structures [Á. Nemcsics *et al*, Mat. Sci. Eng. B **165** 118-121 (2009)]. Few particular behavior of their growth kinetics is also explained [93], [Á. Nemcsics *et al*, Microel. Reliab. (2010) in press]. The QD and QR structures are also investigated by photoluminescence (PL) method [Á. Nemcsics *et al*, phys. stat. sol. c (2010) in press].

LPE growth and optical investigation of InGaAsP/InP double heterostructure wafers

V. Rakovics

GaInAsP/InP is an ideal material system for the fabrication of double heterostructure devices. As InP has higher bandgap than the lattice-matched GaInAsP active layer, absorption losses inside the device structure can be minimized. Liquid phase epitaxy (LPE) was used for the development of device structures, as the composition of the active layer can be relatively easily adjusted by weighing appropriate amount of the materials into the growing melts.

Photoluminescence (PL) is widely employed as a non-destructive characterization technique for epitaxial device structures, yielding measurements that may be correlated with final device performance. In order to obtain useful correlations, however, a number of experimental factors must be considered. We discuss herein the effect of probe source wavelength on the results of experiments. InGaAsP/InP double heterostructure diode wafers (Fig. 1.) grown by liquid phase epitaxy were characterized by photoluminescence and infrared transmission measurements.

Double heterostructure InGaAsP/InP diodes were grown in a computer-controlled LPE apparatus equipped with a multibin slider boat. Single-phase melts with relatively high supersaturations were used for all growth experiments. Four-layer structures were grown on (100) oriented InP substrate consisting of an n-InP buffer layer (3–4 μm), an undoped GaInAsP active layer (1–2 μm), a p-InP confinement layer (6–10 μm), and a p⁺ InGaAsP contact layer (0.5–1 μm). PL and IR transmission spectra have been measured by a fiber optic diode array spectrometer. Tungsten halogen lamp source was used for transmission measurements.

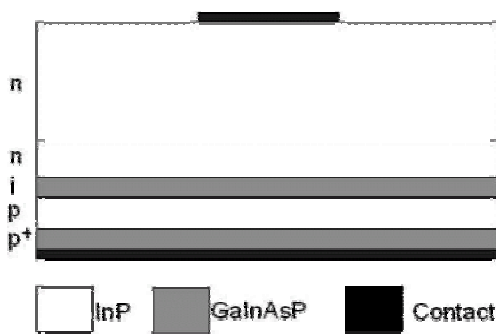


Figure 1 Schematic cross-section of an InGaAsP/InP double heterostructure diode.

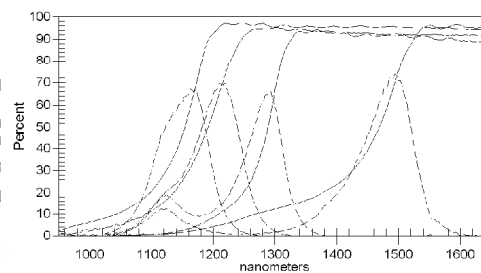


Figure 2 IR transmission and photoluminescence spectra of 1180, 1220, 1290, and 1500 nm LED wafers. The dashed lines show the luminescent spectra at 1120 nm excitation wavelength.

Fig. 2. shows that information obtained from luminescence and infrared transmission are compatible regarding active layer compositions, but in the case of thick active

layers the thickness and compositions of quaternary contact layers remain hidden in transmission measurements, as the active layer is not transparent for higher energy photons.

The optical band gap of direct band gap semiconductors can be obtained from their optical absorption spectrum using $\alpha = A((h\nu - E_g)^{1/2})/h\nu$, where α is the absorption coefficient, A is a constant, $h\nu$ is the energy of the absorbed light, and E_g is the band gap. PL peaks corresponding to 1180 nm contact layer are also not appearing in the spectra. As it is shown in Fig. 3, complex and informative luminescent spectra have been obtained by using visible sources for excitation of InGaAsP/InP double heterostructure diode wafers. The thin contact layer transforms the high energy exciting light to lower energy photons which can excite the active layer, although the InP confining layers are not transparent for primary exciting photons. The peaks corresponding to the active and the contact layers are clearly seen, but with smaller intensity. Intensity ratio of the corresponding active and contact layers is influenced by their thicknesses, and is also affected by the excitation wavelength. Fig. 4 shows the PL spectra of 1510 nm LED wafer at three different excitation wavelengths.

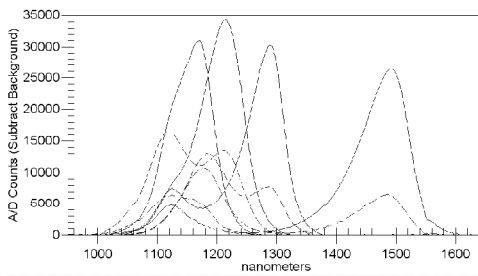


Figure 3 PL spectra of InGaAsP/InP heterostructure wafers. Solid (dashed) lines show the spectra with 1120 nm (525 nm) excitation wavelength.

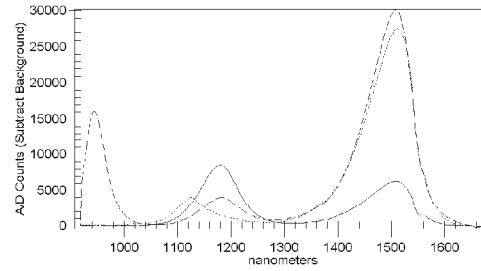


Figure 4 PL spectra of InGaAsP/InP double heterostructure LEDs with 1510 nm active and 1180 nm contact layers. Excitation wavelengths: 1120, 940, and 525 nm for dotted, dashed, and solid lines, respectively.

The two short wavelength peaks are only side effect of the scattering excitation light from the back side of the wafer, but both characteristic peaks can be observed at visible and near infrared excitation. The peak wavelengths obtained by the evaluation of the PL spectra measured with two different excitation sources are practically the same values. In summary, PL intensity spectra are influenced by absorption and energy transfer between the quaternary layers. The peak positions are precisely indicating the composition of the lattice-matched quaternary layers, but for determination of the layer thicknesses an additional measurement, such as optical transmission, is necessary. After the calibration of the PL peak intensity ratios with the quaternary layer thicknesses, the PL measurement is suitable for the quality control of InGaAsP/InP double heterostructure wafers.

Reactive deposition epitaxy growth and electronic properties of iron silicide nanoparticles on Si(001)

(OTKA K81998)

G. Molnár, L. Dózsa, and Z. Vértesy

Future generation thin film solar cells have to use abundantly available, non toxic and environmentally friendly chemical elements. Semiconducting β -FeSi₂ is a possible material which has 23% theoretical efficiency in solar cells, and both its layer and nanoparticle forms have potential applications in photovoltaic technology. Recently, a composite β -FeSi₂/Si film was proposed for photovoltaic use, where charge carriers are generated in the iron silicide particles, which has high photoabsorption coefficient, and the carrier transport takes place in silicon. The motivation of our research was to find proper methods for the preparation of β -FeSi₂ nanostructures.

The iron silicide samples were prepared by reactive deposition epitaxy (RDE), where iron particles were deposited onto heated substrates. The phases and structures were characterized by reflection high energy electron diffraction (RHEED), scanning-(SEM) and transmission electron microscopy (TEM), atomic force microscopy (AFM), and by Fourier transform infrared spectroscopy (FTIR). The electrical characteristics were investigated by I-V and C-V measurements and the defects were measured by DLTS [Vouroutzis N *et al*, J. Alloys Comp. **448** 202 (2008), and Tsormpatzoglou A *et al*, J. Appl. Phys. **100** 074313 (2006)].

The iron silicide nanoislands were successfully grown by RDE on Si(001) substrate. The size distribution and shape of the formed islands depend on the amount of deposited iron and on the annealing after deposition. Using higher temperature and longer time annealing a greater fraction of iron silicide transforms into the β -FeSi₂ phase.

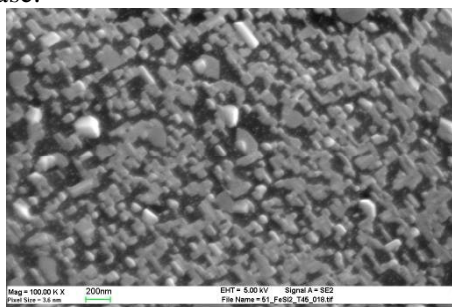


Figure 1 SEM image of a sample with 3 nm deposited Fe thickness.

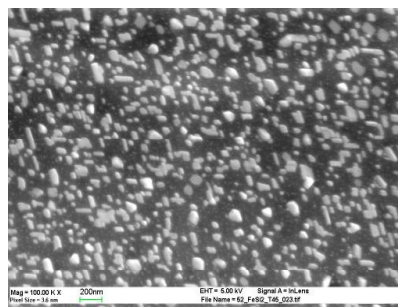


Figure 2 SEM image of a sample with 1 nm deposited Fe thickness.

The size of the dots increases with the annealing time as a consequence of Ostwald ripening and coalescence. To optimize the islands size and β -FeSi₂ phase content further experiments are needed. In case of successful experiments, iron silicide nanostructures may be used as environmentally friendly more effective solar cells.

The detection and identification of contamination in silicon is of technological importance. For understand the electrical properties of nanostructures high spatial resolution is necessary. In this work we used a new method of point defect identification [Dózsa L *et al*: Scanning tip measurement for identification of point defects, accepted for publication in Nanoscale Research Letters]. The electrical characteristics are measured by a DLTS system using a preamplifier. The method is illustrated by measurements performed on iron silicide nanostructures. Fig. 3 shows the detection of Fe-related deep level defects through a series of frequency scan DLTS spectra measured on large-area Schottky junctions.

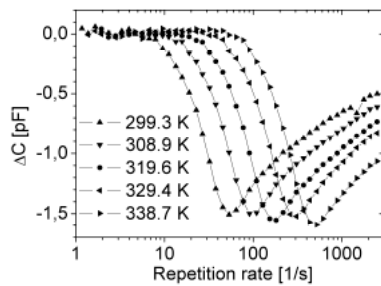


Figure 3 DLTS frequency scan spectra measured in a DLS-83D system at different temperatures.

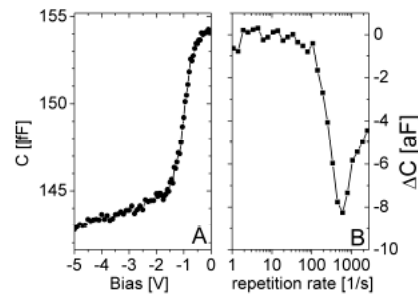


Figure 4 C-V characteristics (A) and DLTS frequency scan (B) measured on a tungsten tip positioned at tunneling distance from the surface.

Capacitance-voltage characteristics and capacitance DLTS frequency scan of the measuring tip positioned at tunneling distance from the silicon surface is shown in Fig. 4. Both the C-V and DLTS characteristics are analogous to characteristics measured in macroscopic Schottky junctions. The preamplifier increases the capacitance sensitivity 200 times, while the current sensitivity increases 1000 times, which enables DLTS measurements on scanning tip-semiconductor junctions.

Reorganization of silica nanoparticles under ion irradiation

(Bilateral project HR-20/08)

Z. Zolnai, S. Lugomer, A. L. Tóth, and I. Bársony

Recent modern topics of nanoscience and nanotechnology relate to the hexagonally ordered mono- and multilayers of silica nanoparticles, which can be considered as e.g. tunable photonic crystals or nanomasks used for modification of the optical, electrical, magnetic or structural properties of macroscopic surfaces at the nanoscale by low energy ion bombardment [N. Nagy *et al*, Appl. Phys. Lett. **89** 063104 (2006)]. Beyond surface patterning, these nanofabrication processes are accompanied by the reorganization of the silica monolayer due to ion-particle and particle-particle interactions, see Fig. 1. Our motivation was to shed more light on this process observed under ion bombardment, and its dependence on the nanoparticle size and ion fluence. The low energy (30 keV) scanning focused Ga^+ ion beam (FIB), as a commonly applied nanofabrication tool, has been used to irradiate the silica monolayers.

We show that the induced patterning of silica particles can be associated with their charging, Coulomb repulsion and motion, heating/surface melting, discharging, particle-particle and particle-substrate adhesive interactions, and causing their reorganization into chain-like clusters [S. Lugomer *et al*: Self-organization of silica nanoparticles induced by the ion beam, to be published in phys. stat. sol. a (2011)]. The calculation of charge accumulation is based on a previous experiment [S. Yogev *et al*, J. Appl. Phys. **103** 064107 (2008)] where the surface potential change induced by FIB was measured with Kelvin probe microscopy on planar silica layers.

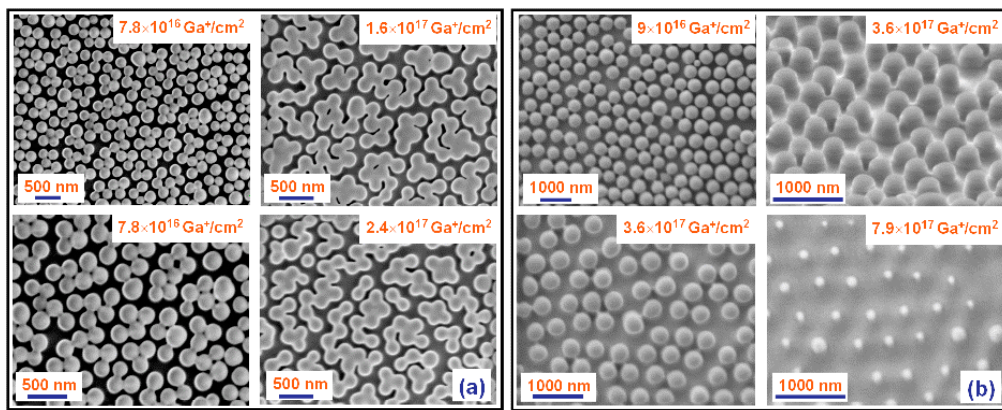


Figure 1 Reorganization of silica nanoparticles under ion irradiation. (a) $D = 220$ nm; Hexagonal layer restructured into isolated clusters (top left); □ Characteristics of chain-clusters (bottom left); Short chain-clusters (top and bottom right); Significant rearrangement occurs. (b) $D = 450$ nm; Disturbed hexagonal layer (□top left); Characteristics of disturbed layer (bottom left); Buckling (side view, top right) and sputtering (bottom right) of particles. Significant rearrangement does not occur.

The high local ion flux of FIB with an input power density of about $1\text{--}10\text{ kW cm}^{-2}$ causes the fast heating of the particles so that the temperature of 2D surface melting of silica is reached within a short time. At high temperature the particles are softened and they can establish significant adhesion contact with each other and with the substrate. The number of particles N , connected into a chain-cluster strongly decreases with the particle diameter D , in the sub-micron size region, see Fig. 2(b). Note further experiments performed by low energy Ar^+ bombardment are under evaluation in order to see the role of the heating rate in final pattern formation.

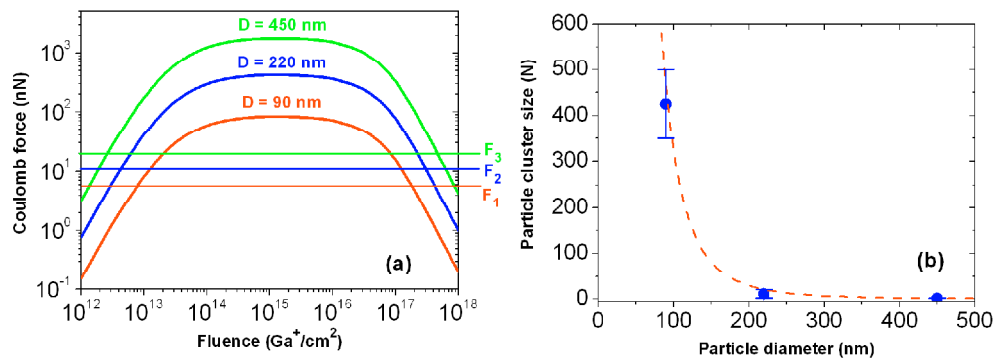


Figure 2 (a) Calculated irradiation-induced Coulomb force vs. ion fluence for $D = 90$, 220 and 450 nm silica particles. F_1 , F_2 , and F_3 denote the corresponding threshold forces (particle-substrate adhesion shear forces) for the motion of silica spheres due to Coulomb repulsion. (b) Cluster-size distribution as function of particle diameter.